

# The Giant Radio Galaxy MRC B0319-454: Circumnuclear Structure of the Host Galaxy ESO248-G10

J. J. Bryant<sup>1</sup>

*School of Physics, The University of Sydney, NSW 2006, Australia.*

and

R. W. Hunstead<sup>2</sup>

*School of Physics, The University of Sydney, NSW 2006, Australia*

## ABSTRACT

We present optical and near-infrared images and spectra of ESO248-G10, the host of the giant radio galaxy MRC B0319-454. From near-infrared colours, the active nucleus is shown to be reddened by hot dust emission or dust extinction. Star forming regions are identified beyond a radius of 5 arcsecs (8.1 kpc) where hot gas is prevalent. The optical spectrum shows gas rotation at speeds of up to  $\sim 350 \text{ km s}^{-1}$  out to  $\geq 32 \text{ kpc}$  along the radio axis. A model is proposed in which the giant elliptical is triaxial with the radio axis along the short axis, and the figure rotation is around the long axis. From the model, the angles of the principal axis are  $\psi = 34^\circ$ ,  $\theta = 65^\circ$ , and  $\phi = 19^\circ$  with axis ratios of  $B/A = 0.75$  and  $C/A = 0.69$ . A second velocity feature from 5 to 15 arcsecs to the north-east of the nucleus is proposed to be a merging gas-rich galaxy inducing star formation while settling into an orbit about the figure rotation axis.

*Subject headings:* galaxies:active — galaxies:elliptical and lenticular, cD — galaxies:individual:ESO248G10 — galaxies:kinematics and dynamics — galaxies:nuclei — infrared:galaxies

---

<sup>1</sup>jbryant@physics.usyd.edu.au

<sup>2</sup>rwh@physics.usyd.edu.au

## 1. INTRODUCTION

Radio galaxies are frequently found to have giant ellipticals as their hosts (Carballo et al. 1998 and references therein). In elliptical hosts with a dust lane, the radio jets are typically aligned perpendicular to the dust lane (Kotanyi & Ekers 1979; Mollenhoff, Hummel & Bender 1992). The sense of rotation of the dust lane about the radio jet axis can be parallel, anti-parallel or perpendicular to the stellar rotation in a stable system. This implies an external origin for the dust. The common occurrence of dust lanes in elliptical galaxies suggests that infalling dust has been trapped in stable closed orbits. It is not surprising, therefore, that Heckman et al. (1986) found that 50–75% of radio galaxies show evidence of ongoing or past mergers/interactions. The orientation of the radio axis and rotation of a dust lane compared to the stellar rotation are indicative of the merger history of the galaxy.

Many elliptical galaxies show evidence of complex kinematics. Warped dust lanes, radio jets misaligned with the major and minor isophotal axes, and tumbling around an axis perpendicular to the radio axis are all indicative of triaxiality in elliptical galaxies. While a warped dust lane could indicate that the dust has not yet settled into a preferred plane, van Albada, Kotanyi & Schwarzschild (1982) have modelled warped dust lanes as stable orbits in tumbling triaxial systems. Binney (1978) first proposed that elliptical galaxies might be triaxial. Since then it has come to be accepted that most, if not all, ellipticals are triaxial and many also show evidence of tumbling. Unfortunately, the intrinsic shape and orientation of such a system cannot be determined from surface photometry alone. While the apparent axis ratios can put limits on the lengths of the intrinsic axes, stellar and ionised gas kinematics together with the dust lane orientation are essential for the determination of a triaxial shape, as they trace the gravitational potential.

MRC B0319–454 is a giant radio galaxy with an FR II (Fanaroff & Riley 1974) morphology. It was identified by Jones (1989) with the Molonglo Observatory Synthesis Telescope (MOST). The double-lobed radio structure has a projected separation of 2.51 Mpc ( $H_0 = 50 \text{ km s}^{-1} \text{ Mpc}^{-1}$ ), with quasi-continuous jets at a position angle of  $51^\circ$  and radio knots mapped by Saripalli, Subrahmanyan & Hunstead (1994). The host galaxy, ESO248-G10, has been identified with a

giant elliptical galaxy at a redshift of 0.0625, giving a distance of 337 Mpc. At this distance 1 arcsec corresponds to 1.63 kpc. With a major axis of  $\sim 100 \text{ kpc}$  at the  $R = 24.5 \text{ mag arcsec}^{-2}$  contour, it is an ideal candidate to investigate the host galaxy properties of a giant radio galaxy.

The optical images of Saripalli et al. (1994) show ESO248-G10 to have a warped dust lane. The radio axis is misaligned with the optical isophotal minor and major axes by  $34^\circ$  and  $56^\circ$  respectively, hinting that the galaxy may be triaxial. In this paper we attempt to deduce the true orientation of the principal axes to the apparent isophotal axes from the dust lane morphology and ionised gas dynamics. Furthermore, colour analysis is used to find direct evidence of a merger or interaction. Section 2 describes the observations and reduction, with the results in section 3. A discussion of the dynamics and orientation of ESO248-G10 is in section 4.

## 2. OBSERVATIONS AND REDUCTION

### 2.1. Images

The near-infrared bands of  $J$ ,  $H$ , and  $Kn$  are ideal for studying the circumnuclear regions of ESO248-G10 as infrared wavelengths can penetrate the enshrouding dust. Mosaiced images centred on the nucleus of ESO248-G10 were taken in  $J$ –,  $H$ –, and  $Kn$ –bands (see Table 1). The  $Kn$  image was obtained with IRIS (Allen 1992) at the f/15 cassegrain focus of the 3.9 m Anglo-Australian Telescope (AAT) at Siding Spring Observatory on 1994 October 22. Pixels were 0.6 arcsec on the sky, with  $128 \times 128$  pixels on the HgCdTe array. The mosaic was comprised of three, five-point patterns centred on the  $Kn$  point source with offsets of between 10 and 15 arcsec for the surrounding frames. The standard star HD20223 was observed immediately after the image frames. Sky frames were offset by between 80 and 190 arcsec from the galaxy centre.

$J$  and  $H$  images were taken with CASPIR (McGregor et al. 1994) on the MSSSO 2.3 m telescope at Siding Spring Observatory on 1998 October 1-2 and 1999 February 4 respectively. The  $256 \times 256$  InSb array was used in FAST mode with 0.5 arcsec pixels. A nine-point pattern of images made up both the mosaics, with offsets of 8 arcsec for each frame surrounding the nucleus. Sky frames were offset by 300 arcsec from the nucleus. The standard stars HD20223 and HD15911 were observed immediately before or after

Table 1: Log of Observations.

UT Date	Type	$\lambda$	Av. Seeing (arcsec)	Photometric	Integration Time (s)
1994 Oct 22	image	Kn	1.4	Yes	750
1999 Feb 4	image	H	1.3	Yes	1000
1998 Oct 1-2	image	J	1.5	Yes	1740
1995 Feb 7	spectrum	Opt.	1.25	Yes	2000
1995 Oct 31	spectrum	HK	2.5	No	11640

the image frames.

Data reduction and image processing was done with four software packages: IRAF (Tody 1993), FIGARO (Shortridge 1993), KARMA (Gooch 1996), and MIRIAD (Sault, Teuben & Wright 1995). The  $Kn$ -band IRIS image was reduced with the IRIS-specific tasks in FIGARO, while the  $J$  and  $H$  images used the CASPIR reduction package in IRAF. In each case the frames were flat fielded using dome flats and then sky-subtracted. All three wavebands were cleaned of bad pixels with FIGARO CLEAN and mosaiced with IRIS-MOS. At least four stars in the field were used to register the frames when mosaicing the  $J$  and  $Kn$  images. The  $H$  image, however, was taken with tip-tilt correction and blind mosaicing was sufficient. All three images were taken in photometric conditions and were magnitude calibrated using the standard star observations.

### 2.1.1. Alignment of Images

The  $J$ ,  $H$ , and  $Kn$  images were aligned relative to each other by the following method. The  $Kn$  image was resampled from  $0.6 \text{ arcsec pixel}^{-1}$  to  $0.5 \text{ arcsec pixel}^{-1}$  with IRAF MAGNIFY to match the  $J$  and  $H$  images. By cross-referencing six stars on the digitized sky survey (DSSI, blue) image in KARMA KOORD, coordinates were attached to the  $J$  mosaic accurate to  $0.1 \text{ pixel rms}$ . Coordinates were transferred to the  $H$  and  $Kn$  images in the same way but the  $Kn$  image was smaller so that fewer alignment stars gave a larger scatter. It was then necessary to shift the  $H$  and  $Kn$  images with IRAF IMSHIFT to align the relative pixels to the  $J$  image to  $< 0.2 \text{ pixel}$ .  $J - H$  and  $H - Kn$  magnitude images were then made in MIRIAD by subsetting an identical region from each of the images, then converting to magnitude images and subtracting. A coordinate system was applied to  $H - Kn$  and  $J - H$  images by copying the fits header parameters from the parent images.

The  $B$  and  $R$  CCD images were those used by Sari-palli et al. (1994). They were taken at the AAT, and are measured to have a seeing disk FWHM of  $2.65 \text{ arcsec}$  and  $1.8 \text{ arcsec}$  for  $B$  and  $R$  respectively. Coordinates were transferred to both images by comparison with the DSS image. The resulting images align with the  $J$  image to  $< 0.2 \text{ arcsec}$ . The  $R$  image was convolved to have the same resolution as the  $B$  image, before a  $B - R$  image was made with the same relative astrometric accuracy.

## 2.2. Spectra

### 2.2.1. Optical

Optical spectra were taken for us as service observations at the AAT on 1995 February 7 (see Table 1). The RGO spectrograph was used with the 25cm camera, 270R grating, and Tektronix  $1k \times 1k$  CCD. The slit was  $192.5 \text{ arcsec}$  long with a spatial scale of  $0.76 \text{ arcsec pixel}^{-1}$ ; it was aligned at a position angle of  $40^\circ$ , rather than the requested  $51^\circ$  (radio jet axis p.a.) and consequently is not along any physically significant direction. Sky subtraction and cosmic ray removal was done in FIGARO. Wavelength calibration was done with CuAr lamp spectra and the measured spectral resolution is  $7.5 \text{ \AA}$  FWHM. The resultant spectral image shows significant rotation in the stronger emission lines  $[\text{N II}]\lambda 6584$  and  $\text{H}\alpha$ , which can be seen in Figure 1(a)&(b). Spectra were therefore extracted along the slit to measure the velocities either side of the nucleus. To improve the signal-to-noise ratio away from the nucleus an increasingly wide extraction window was used. A 3-pixel spectrum was extracted at the centre, then spectra with 3, 4, 4, 5, 5, and 5 pixels were extracted consecutively to the north-east, and 3, 4, 4, and 5 pixels similarly to the south-west. Two more spectra of 9 pixels each were centred 19 pixels north-east and 18 pixels south-west of the centre. Each of the resulting spectra was divided by that of the standard star HD26169. From

each of these spectra, the  $[\text{N II}]\lambda 6584$  and  $\text{H}\alpha$  lines were deblended with IRAF NGAUSSFIT by constraining the relative flux, position and width of the  $[\text{N II}]\lambda 6584$  &  $6548$  lines. Other lines were measured with IRAF SPLIT. Figure 1(c) shows the rotation curve formed from the  $[\text{N II}]\lambda 6584$  and  $\text{H}\alpha$  line velocities measured from each of the extracted spectra. Each point on the curve is plotted at the center of the extracted window that formed each of the 13 spectra. It is noteworthy that the lines could be measured to a radius of  $\sim 20$  arcsec to the north-east, but only  $\sim 14$  arcsec to the south-west. The S/N in the  $\text{MgIb}$  line was not sufficient to measure a stellar rotation curve.

Optical extinction is typically measured from the  $\text{H}\alpha/\text{H}\beta$  ratio. The  $\text{H}\beta$  line is, however, not measurable with sufficient accuracy to give a meaningful estimate of extinction. Furthermore, as the nucleus is below the highest obscuration of the dust lane (see section 3.1), extinction correction was not applied to the emission line measurements. The errors in the  $[\text{N II}]\lambda 6584/\text{H}\alpha$  line ratios due to extinction are negligible as the wavelengths are close. Figure 1(d) shows the  $[\text{N II}]\lambda 6584/\text{H}\alpha$  ratios for five of the spectra. These ratios will be discussed further in section 4.2.2.

### 2.2.2. Near-infrared

An HK echelle spectrum was obtained with IRIS on the AAT on 1995 October 31. The wavelength coverage is from 1.45 to  $2.5\mu\text{m}$ , with a resolution of 400. The slit was 13 arcsec long, with a spatial scale of  $0.79$  arcsec pixel $^{-1}$ , and oriented east-west. The galaxy nucleus was positioned 3.5 arcsec either side of the centre of the slit in alternate frames. Typical IRIS reduction involves subtraction of pairs of frames to remove sky and background galaxy. While this method was used here, it was discovered later (see section 4.2.2) that beyond 4 arcsec from the nucleus along the optical slit angle, the galaxy has starburst processes not found at the nucleus. Starbursts regions may also be present in the direction of the HK slit, at a radius of 7 arcsec from the nucleus, in the region used for sky subtraction. There is therefore a chance that the sky background spectra that were subtracted may have starburst lines not found at the nucleus. However, contribution from these possible lines is expected to be small, as the nucleus is so much brighter than the background galaxy. This possible contamination is taken into account in evaluation of the spectrum.

The echelle frames were flat-fielded and cleaned in

FIGARO. After coadding, spectra were extracted from the central 4 pixels. Two standard stars bs1006 and HD21473 were used to flux calibrate the spectrum with IRISFLUX. As the observing conditions were not all photometric, this flux calibration is only relative. Wavelength calibration was done with argon lamp spectra and wavelengths were corrected to a heliocentric frame.

## 3. RESULTS

### 3.1. Images

In Figure 2, the  $R$  image shows a dust lane crossing the front of the galaxy to the north-east of the nucleus. This suggests the galaxy is tilted away from the sky plane to the north-east. The nucleus is therefore positioned below the strongest band of extinction. The near infra-red images are much more centrally condensed, with the  $Kn$ -band image having an unresolved core coincident, within errors, with the radio core reported by Saripalli et al. (1994). The  $J$  image shows a notch-shaped indentation approximately 4 arcsec to the east of the nucleus, which is not apparent in the  $H$  and  $Kn$  images. Overlaid  $J - H$  and  $H - Kn$  extinction images formed from the division of the  $J$ ,  $H$ , and  $Kn$  images are shown in Figure 2(d). As expected, the strongest reddening in the  $H - Kn$  image is above the nucleus, along the dust lane.

Aperture photometry results are given in Table 2. Apertures were chosen to extend well past the north-east edge of the dust lane, with measurements made using the IRAF RADPROF program. All apertures are centred on the  $Kn$ -band peak, which coincides, within errors, with the peaks in  $J$ - and  $H$ -bands. As a background aperture is required for photometry, and the three images are different sizes, an annulus was chosen that fits within each image and avoids any stars. With inner and outer radii of 36 and 41 arcsec, this background aperture avoids the main galaxy halo, but a small contribution from the galaxy cannot be ruled out. At large apertures, this introduces an estimated systematic error of up to 0.1 magnitudes. In smaller apertures, however, the error is dominated by standard star photometry errors, which are 0.02 magnitudes.

Aperture photometry in  $Kn$ -band gave the absolute magnitude in a 1.5 arcsec radius aperture as  $M_K = -25.9 \pm 0.5$ . The canonical luminosity criteria for optical QSOs is  $M_K = -25.8$  (Surace & Sanders 1999), while typical Seyferts only have  $M_B = -20.2$ .

MRC B0319-454 [NII]  $\lambda$ 6584 & H $\alpha$  Rotation Curve

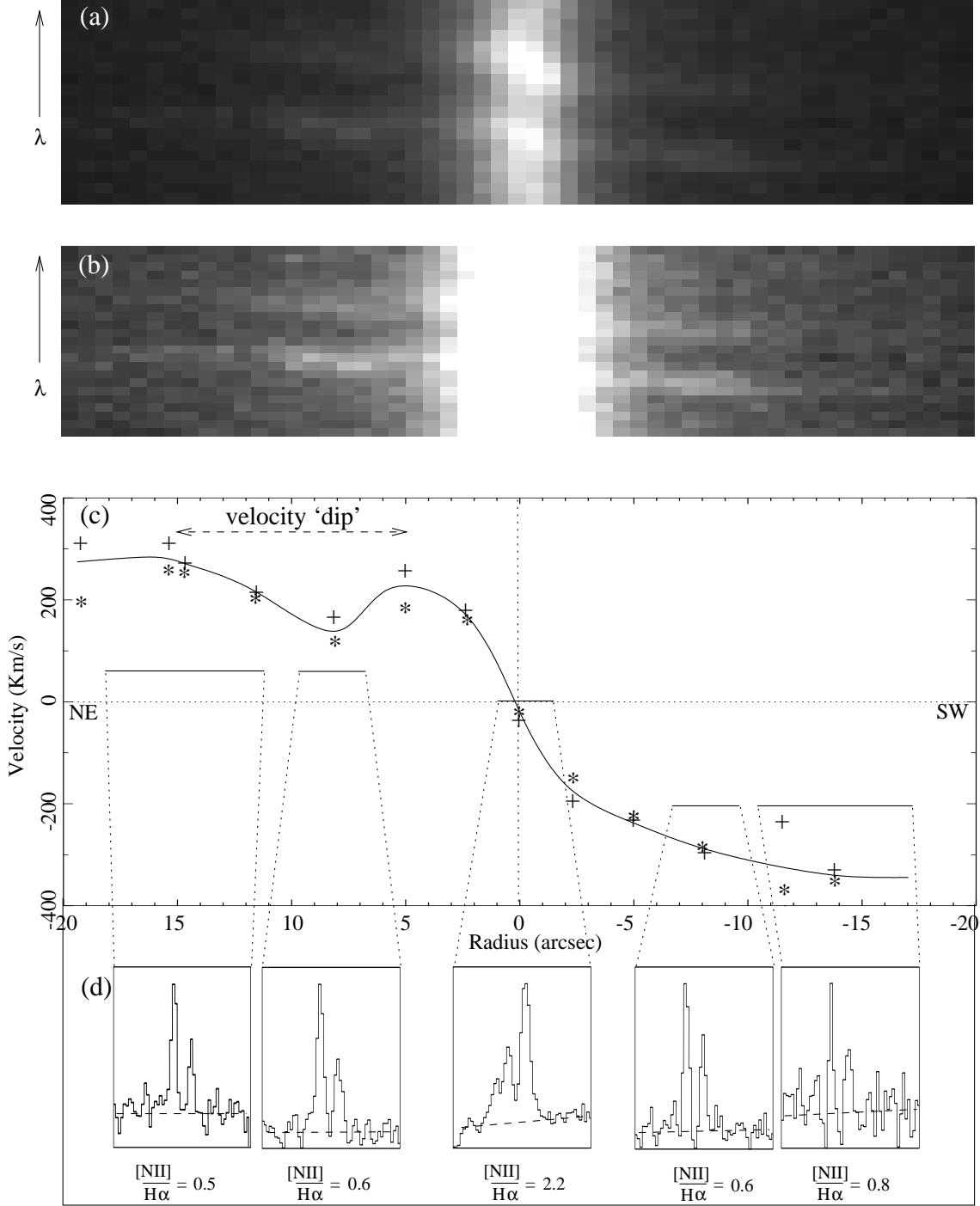


Fig. 1.— (a) Optical Spectral Image including the [NII]  $\lambda$ 6584 and H $\alpha$  lines. The inner pixels clearly show fast rotation of  $\sim 100$  km s $^{-1}$  arcsec $^{-1}$ . (b) Same as (a) with greyscales chosen to highlight the extent of the rotating gas out to almost 20 arcsecs. (c) Rotation Curves for [NII] (crosses) and H $\alpha$  (stars) along p.a. of 40°. See text for explanation of the points. (d) Change in the relative strength of [NII]  $\lambda$ 6584 and H $\alpha$  with position. Each spectrum is for the region marked by the corresponding line on the rotation curve and has a width of  $\sim 182$  Å.

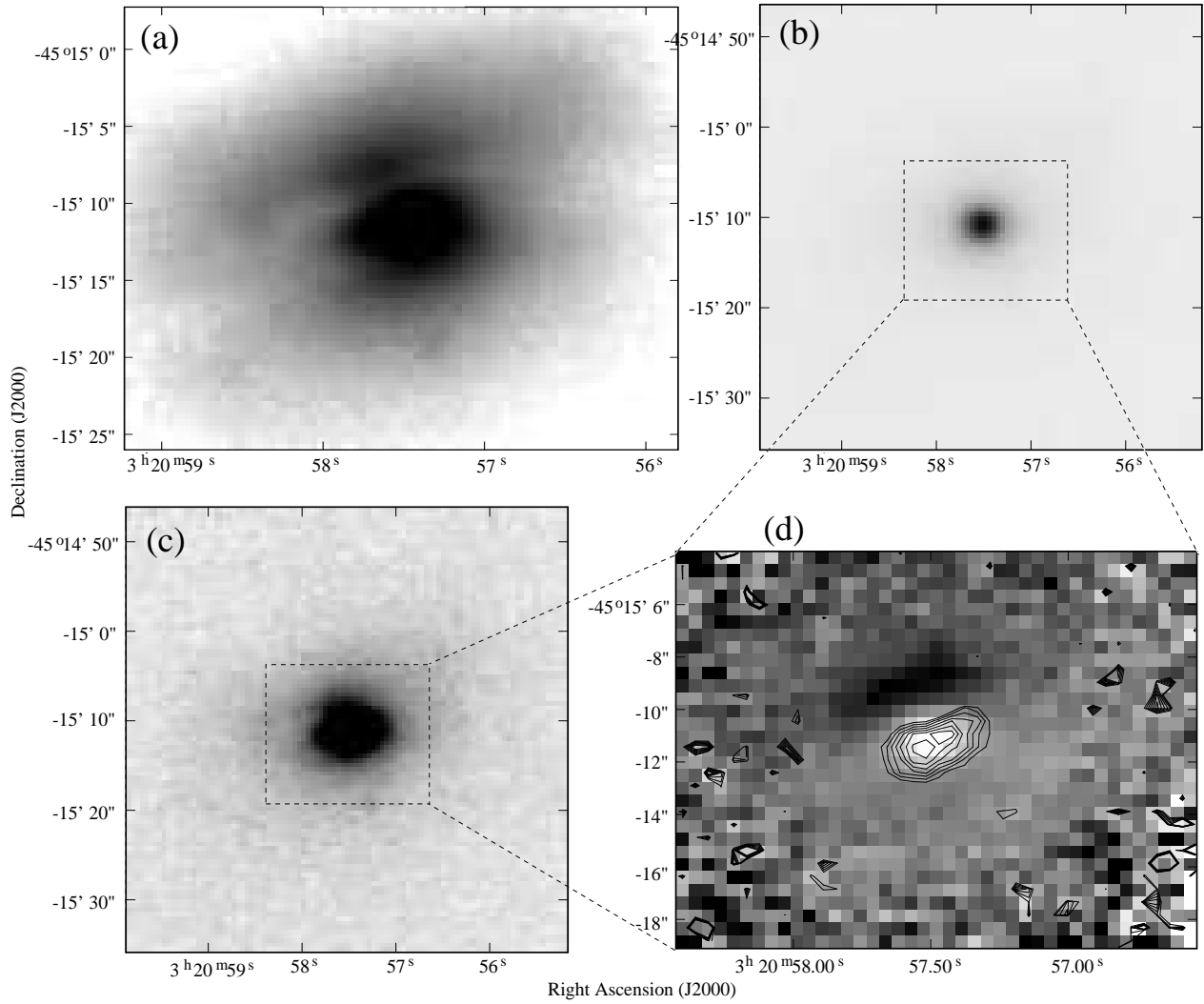


Fig. 2.— (a)  $R$ , (b)  $Kn$ , and (c)  $J$  band images. (d)  $H - Kn$  extinction image, with overlaid contours of the  $J - H$  extinction image; darker regions indicate greater reddening. Contour levels are 0.86-0.98 in 0.02 steps.

Table 2: Aperture photometry centred on the IR point source. Errors in the colours range from 0.02 – 0.1 mag from smallest to largest apertures.

Aperture	Radius (arcsec)	<i>J</i> (mag)	<i>H</i> (mag)	<i>Kn</i> (mag)	<i>J</i> – <i>H</i> (mag)	<i>H</i> – <i>Kn</i> (mag)
1	15.24	14.30	12.66	0.94	1.65	
2	14.24	13.35	11.47	0.89	1.89	
3	13.82	12.96	10.94	0.86	2.02	
4	13.54	12.71	10.64	0.83	2.07	
5	13.35	12.54	10.45	0.81	2.09	
6	13.19	12.40	10.30	0.79	2.10	
7	13.07	12.30	10.18	0.77	2.11	
8	12.96	12.21	10.09	0.76	2.12	
9	12.88	12.13	10.01	0.74	2.13	
10	12.80	12.07	9.94	0.73	2.13	

Therefore, the infrared light from ESO248-G10 is sufficient to class it with the QSOs.

### 3.2. Spectra and Rotation Curves

#### 3.2.1. Emission Lines and Ratios

Figure 3 shows the optical spectrum at the nucleus. The emission lines of  $[\text{N II}]\lambda\lambda 6548, 6584$ ,  $\text{H}\alpha$ ,  $[\text{O III}]\lambda\lambda 4959, 5007$ ,  $[\text{O I}]\lambda 6300$ , and  $[\text{S II}]\lambda\lambda 6716, 6731$ , and the absorption lines of  $\text{NaID}$  and  $\text{MgIb}$  are all marked.

In Figure 4, the near-infrared HK spectrum has some absorption lines, but no emission lines are evident. Significant lines that lie within the spectral range at this redshift include two hydrogen recombination lines ( $\text{Pa}\alpha$  and  $\text{Br}\gamma$ ), several  $[\text{Fe II}]$ , and  $\text{H}_2$  lines. Hydrogen recombination lines are expected to be stronger from starbursts than AGNs due to the  $\text{H II}$  regions surrounding young hot OB stars (Hill et al. 1999). This may suggest that there is not a strong contribution from starburst regions within a radius of 1.6 arcsec (the offset of the extracted spectrum) from the nucleus. The lack of  $[\text{Fe II}]$  and  $\text{H}_2$  lines is less indicative as their origins can be starburst or AGN. For starburst regions,  $[\text{Fe II}]$  lines can be excited in the cooling tails of supernova remnants, or directly photoionized by young OB stars. Alternatively, X-rays from the nuclear source may photoionize the NLR clouds, or radio jets may shock-excite iron. In section 4.2.2, we show that the optical line ratios in the nuclear regions provide strong evidence for AGN activity while further out, starburst processes are found.

The lack of  $[\text{Fe II}]$  lines in the nuclear spectrum indicates that the AGN processes are not exciting iron in this galaxy. There may be a lack of iron within 1.6 arcsec of the nucleus, or alternatively, this could point to the starburst processes as more likely to be the excitation mechanism for iron in active galaxies.

#### 3.2.2. Rotation Curves

The ionised gas rotation curve in Figure 1(c) clearly shows fast rotation along the slit direction, which has a position angle  $11^\circ$  from the radio axis. The actual rotation axis is unknown. The south-west side is approaching and the north-east (dust lane) side is receding. As the distribution of emission lines is not symmetric about the nucleus (see section 2.2.1), the ionised gas extends further to the north-east than the south west. The rotation curve shows a sudden decrease in velocity from  $5 \pm 1$  arcsec to  $\sim 15$  arcsec to the north-east. A comparison of the features in Figure 5 shows that the dust lane extends to a maximum offset of  $\sim 4$  arcsec from the nucleus, which is before the decrease in velocity and is therefore unlikely to be related. Similarly, Nicholson, Bland-Hawthorn & Taylor (1992) found that the dust lane obscuration has only a minor effect on an  $\text{H}\alpha$  image of the dust lane elliptical galaxy, Centaurus A. The slowest velocity point in the ‘dip’ does not have a corresponding feature in the ESO248-G10 images.

It is noteworthy that the rotation curve shows no sign of a turnover out to 20 arcsec or  $\sim 3.3$  effective radii. Extended rotation curves have been measured

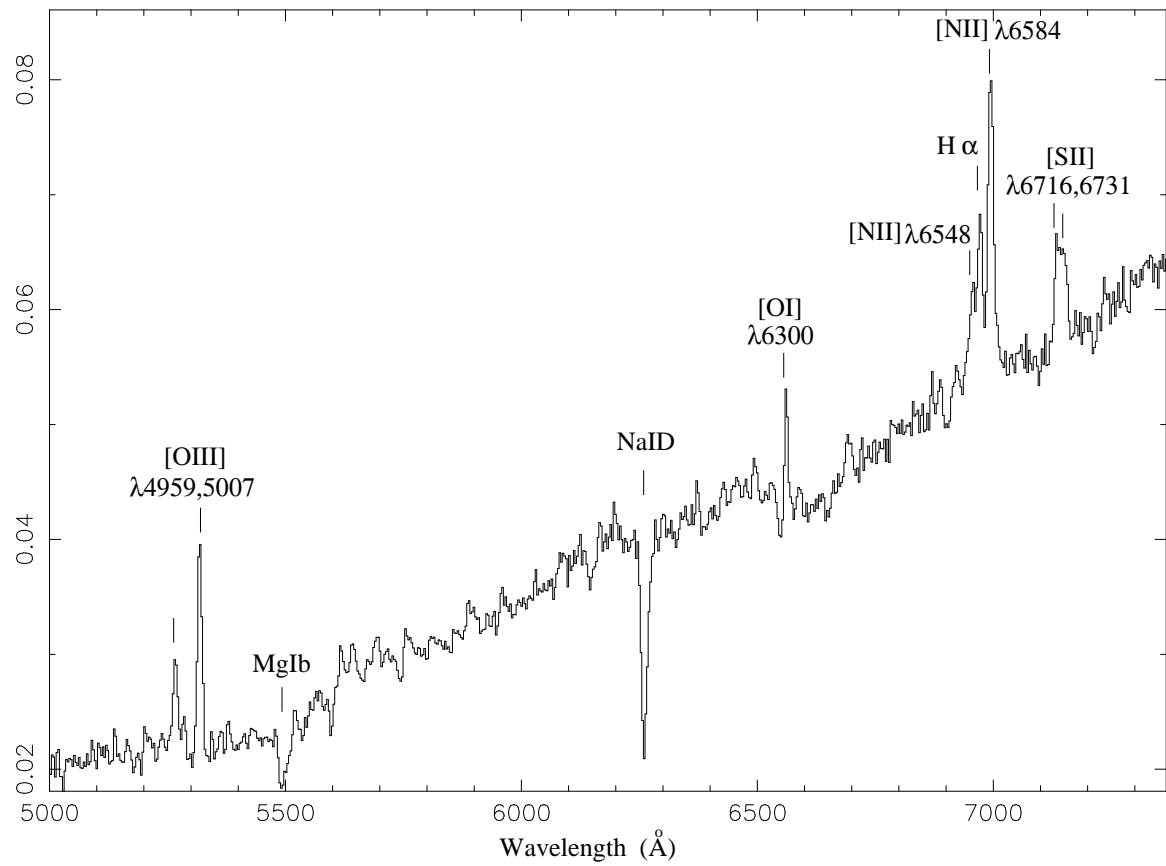


Fig. 3.— The optical spectrum of ESO248-G10 at the nucleus. Relative values only are shown on the intensity scale as the spectrum is not flux calibrated.

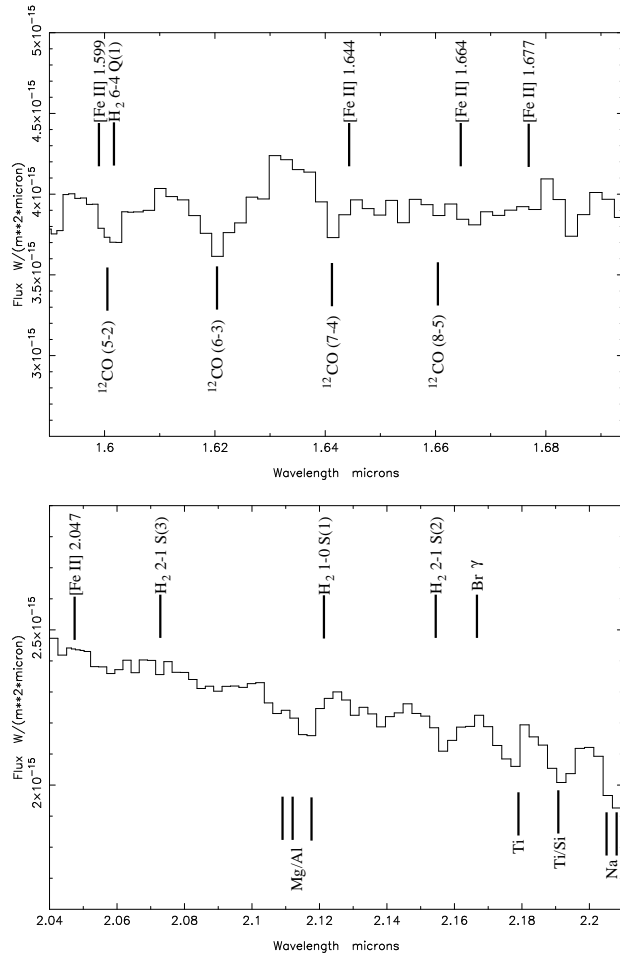


Fig. 4.— Two regions of the near-infrared spectrum are shown, shifted to the rest frame. The expected positions of [Fe II],  $^{12}\text{CO}$ , and  $\text{H}_2$  lines are marked. While some absorption lines are evident, none of the expected emission lines are clearly detected. Typically, the strongest lines would be the [Fe II] lines at  $1.644\mu\text{m}$  and  $1.664\mu\text{m}$  and the  $\text{H}_2 1 - 0 \text{ S}(1)$  line. The wavelength calibration is accurate to  $0.003\mu\text{m}$ .

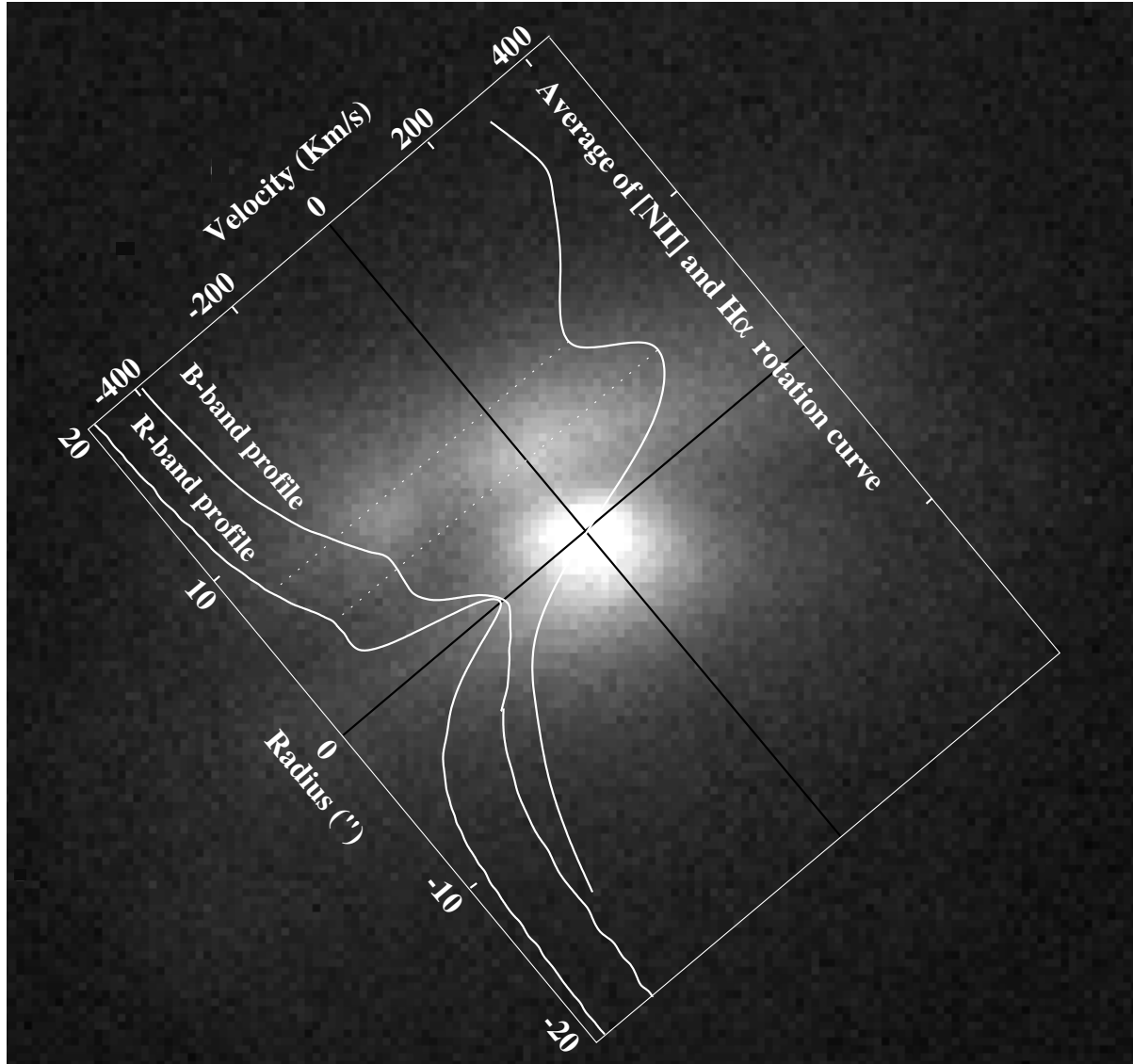


Fig. 5.— Graph of the  $\text{H}\alpha$  and  $[\text{N II}]\lambda 6584$  average rotation curve and the profiles across the  $R-$  and  $B-$ band images along the slit. This is then overlaid on the  $B-$ image such that the graph radius-axis aligns with the slit position angle through the nucleus.

for relatively few ellipticals (e.g. NGC 3115, Capaccioli et al. 1993) and in each case, have been found to remain flat out to 3 – 4 effective radii.

## 4. DISCUSSION

### 4.1. Galaxy Rotation and Orientation

#### 4.1.1. Orientation of the Principal Axes

The emission line gas shows fast rotation along an apparent axis close to the radio axis (Figure 1(c)). Elliptical galaxies with rings or disks rotating about an axis perpendicular to the symmetry plane are not rare. A survey of 40 early-type galaxies with dust lanes by Hawarden et al. (1981), found that polar disk/ring galaxies comprised the largest subgroup, suggesting that they are likely to be stable systems. Such a polar gas disk is only stable in a triaxial system (Steiman-Cameron & Durisen 1982; van Albada et al. 1982). Triaxial galaxies have principal axes  $a$ ,  $b$ , and  $c$  of lengths  $A$ ,  $B$ , and  $C$  such that  $A > B > C$ , where  $A=B$  for oblate and  $B=C$  for prolate ellipticals. Many attempts have been made to find the orientation of the three principal axes with respect to the apparent projection of triaxial galaxies (van Albada et al. 1982; Steiman-Cameron, Kormendy & Durisen 1992 and references therein). The first assumption is that the radio axis is aligned with a principal axis of the system. It is then commonly accepted that the dust lane will lie perpendicular to the radio axis for the following reasons: firstly, there is a strong association between galaxies with radio jets and those with dust lanes, and hence both features are likely to be produced by a related mechanism such as the gas layer fuelling the central accretion disk. Secondly, surveys of galaxies with dust lanes and radio jets have shown a strong correlation between the jet axis and rotation axis of the dust lane disk (Kotanyi & Ekers 1979, Mollenhoff et al. 1992).

Dust lanes and cylindrical gas disks are thought to be the result of mergers, as they are common features of galaxies with boxy bulges (eg: NGC7332, Fisher, Illingworth & Franx 1994), and are often dynamically decoupled from the stellar velocity field (Bertola, Busson & Zeilinger 1992). Steiman-Cameron & Durisen (1982) and Steiman-Cameron et al. (1992) modelled gas in-falling into a triaxial potential from several merger scenarios. They found that the accreted gas from the merger of a gas rich galaxy and an elliptical would settle into one of the principal planes of the

resulting galaxy. The initial orientation of the angular momentum vector of the accreted gas, relative to the principal planes, will determine into which plane it settled through differential precession and dissipation. The angular momentum of the accreted gas can be parallel, anti-parallel or perpendicular to the stellar rotation. If the figure rotation axis lies in the plane of the dust lane, the result is tumbling about this plane. Furthermore, if the gas and dust are from separate merger or interaction events, then the cylindrical gas disk rotation can be perpendicular, parallel or anti-parallel to the dust lane and radio axis.

Attempts to model stable orbits in triaxial potentials have shown that the only stable axes of rotation are the long and the short axes,  $a$  and  $c$  respectively. Rotation about the intermediate axis is unstable (van Albada et al. 1982). If the axis of rotation of the dust disk (and hence the radio axis) is the short axis, then a stable polar gas disk is therefore confined to be orbiting the long axis, and vice versa (Steiman-Cameron & Durisen 1982, Merritt & de Zeeuw 1983). The figure rotation may be parallel or perpendicular to the radio axis but cannot occupy the intermediate axis. If the figure rotation is perpendicular to the radio axis, the triaxial figure is tumbling. Furthermore, if the surface figure is tumbling, it must do so much slower than the orbital period of gas in the polar disk, so the disk will not become unstable. The apparent stability of polar gas disks implies that these galaxies are triaxial and that the surface figure rotates much slower than the polar gas disk.

In order to find stable configurations for rotating triaxial systems, it will be assumed that the figure rotation is in the same sense as the stellar rotation. This applies if the mass distribution follows the light distribution. If so, then the four possible stable configurations are given in Table 3 (Merritt & de Zeeuw 1983, van Albada et al. 1982). The warped dust lane in ESO248-G10 is aligned closest to the major axis (Saripalli et al. 1994). This classifies ESO248-G10 as configuration 3 in Table 3. Hence the radio axis is the short axis and the figure rotation is about the long axis. While the actual gas rotation position angle has not been measured, the spectrum showed fast rotation along the slit at a p.a. of  $40^\circ$ . The radio axis is only  $11^\circ$  away at a p.a. of  $51^\circ$ . Therefore the axis about which the gas orbits is likely to be in, or close to the plane of the dust lane, perpendicular to the radio axis. If the gas is from a recent merger it may not yet have settled into a principal plane. If

the gas orbit has settled and is stable, then the rotation axis is in the plane of the dust disk and confined to the long axis. In that case, the stars and gas are tumbling about the long axis with the figure rotation much slower than that of the gas.

It has been argued that warped dust disks are transient and have not yet settled into their rotation plane. However, van Albada et al. (1982) showed that slow figure rotation or tumbling about an axis in the plane of the dust disk can result in a stable warped disk due to the Coriolis force. The resulting warp increases with radius. Furthermore, if the warped dust lane is along the major axis, then the rotation of the warp is prograde to the figure rotation when viewed down the figure rotation axis (Merritt & De Zeeuw 1983, Kormendy & Djorgovski 1989). While the gas and stars are both rotating about the long axis, the sense of the stellar rotation is unknown. It would be plausible for both to rotate in the same sense, although it is not impossible to find counter-rotation about the same axis (eg. NGC7332, Fisher et al. 1994). If the gas and stars in ESO248-G10 are rotating in the same sense, then its figure rotation is away from the observer to the north-east. A stable system would therefore imply that the south-east dust lane warp is rotating away from the observer. Furthermore, the optical images reveal the strongest extinction from the dust lane is north of the nucleus (Figure 2(a)) and hence the dust lane tilts away from the sky plane to the north-east. As the warp in the dust disk is expected to increase with radius, this confines the long (figure rotation) axis to have a position angle greater than  $107^\circ$  (from the inner dust lane). Furthermore, the projected long axis is likely to be close to perpendicular (p.a. =  $130^\circ$ ) to the slit orientation as the measured velocity is so fast. Figure 6 shows the orientation of the observed axes. The long figure rotation axis is shown at a nominal p.a. of  $119^\circ$ , midway between the above values.

#### 4.1.2. A Model for the Orientation of ESO248-G10

The radio axis is expected to align with the long or the short principal axis (see section 4.1.1). However, due to orientation effects, the radio axis does not appear coincident with the apparent major or minor axes. In such a triaxial system, to determine the orientation of the principal axes and their relative lengths requires five parameters. Firstly, we define  $\psi$  as the apparent angle between the minor axis and the projection of the short principal axis on the

sky. Two more parameters define the principal axes lengths such that  $\zeta = B/A$  and  $\xi = C/A$ . The remaining viewing angles are given by the Euler angles  $(\theta, \phi)$ . We define two coordinate systems in Figure 7: (a,b,c) are the axes associated with a triaxial ellipsoid, while (x,y,z) define the sky plane with z along our line of sight.  $\theta$  is the angle of axis c to the line of sight. The angle from axis a to the intersection of the c-z and a-b planes defines  $\phi$ .

The relationships among these five parameters have been extensively discussed in the literature since Stark (1977) derived the apparent brightness distribution of a set of similar triaxial ellipsoids (see also van Albada et al. 1982; de Zeeuw & Franx 1989). We extend the notation and equations of Hui et al. (1995) to the case of ESO248-G10, where the radio axis is along the short axis, and  $\psi$  is  $34^\circ$  (Saripalli et al. 1994). It can be shown that

$$\xi = \sqrt{0.404 L \cot\theta \cosec\theta - M \cot^2\theta + N \cosec^2\theta}, \quad (1)$$

where

$$M = (\zeta^2 \sin^2\phi + \cos^2\phi), \quad (2)$$

$$N = (\sin^2\phi + \zeta^2 \cos^2\phi), \quad (3)$$

$$L = \sin 2\phi (\zeta^2 - 1) \quad (4)$$

and  $\psi$  is the apparent angle of the short axis to the minor axis as defined above, when

$$M \cos^2\theta + \xi^2 \sin^2\theta - N + 2.475 L \cos\theta \leq 0. \quad (5)$$

We now set about finding values of  $\theta$ ,  $\phi$ ,  $\xi$ , and  $\zeta$  that satisfy equations 1–5. To constrain these four parameters, several assumptions will be made. As the radio structure appears so large (Saripalli et al. 1994), we assume that the radio axis (and hence the short axis) is close to the sky plane, say,  $\theta > 60^\circ$ . However, with the radio axis perpendicular to the dust lane (see section 1), the tilt of the dust lane suggests the radio axis is projected away from the sky plane to the north-east, and hence  $\theta < 90^\circ$ . We therefore adopt  $60^\circ < \theta < 80^\circ$ . There are then two constraints on  $\phi$ . Firstly, for a given  $\theta$ ,  $\phi$  must be chosen to give the correct apparent angle between the figure rotation (long) and radio (short) axes, called  $\beta$ . From section 4.1.1, the figure rotation axis has p.a.  $> 107^\circ$  and the radio axis has p.a. =  $51^\circ$ , therefore  $\beta > 56^\circ$ . Secondly, as  $b > c$ , equation 1 requires that for any given  $\theta$ ,  $\phi$  is limited by  $\zeta > \xi$ . Figure 8 shows the set of curves for which  $\zeta > \xi$ . For any chosen

Table 3: Four possible configurations for rotating triaxial systems.

Configuration	Figure Rotation (Stellar Rotation)	Rotation of Dust Disk (Radio Axis)	Form of Dust Lane and App. Major/Minor Axis	Example
1	short axis	short axis	flat - major	M31
2	short axis	long axis	warped - minor	CenA, M84?
3	long axis	short axis	warped - major	M84?, ESO248-G10
4	long axis	long axis	flat - minor	

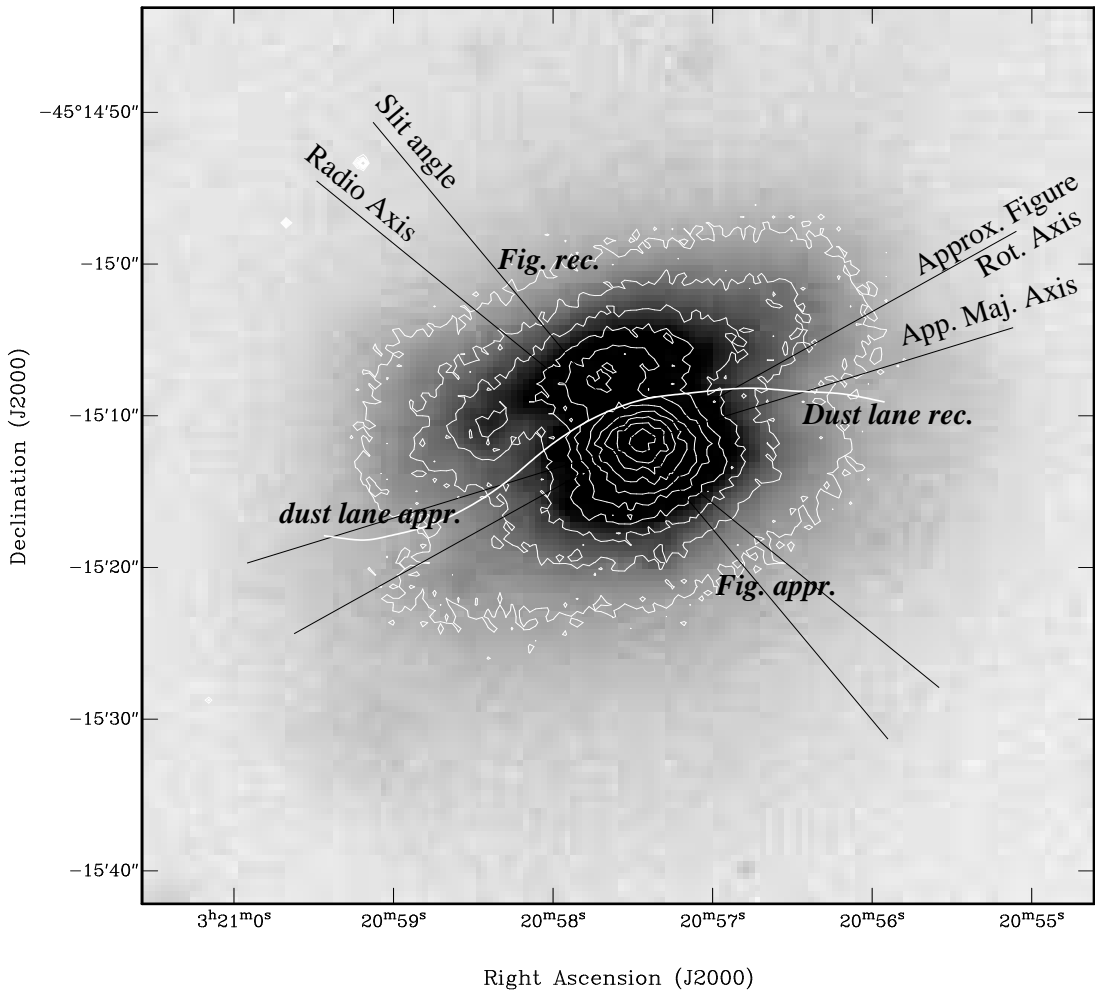


Fig. 6.— Orientation of observed axes overlaid on the  $B$ –band image and contours.

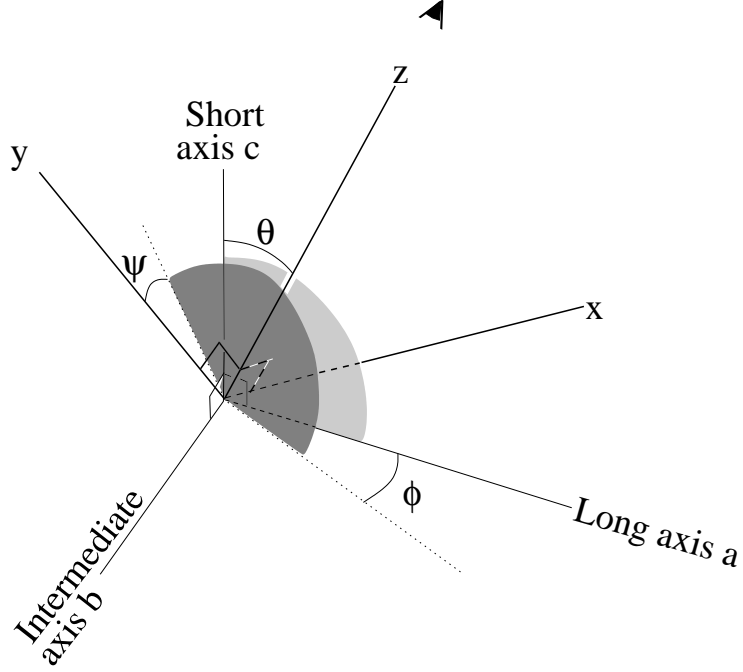


Fig. 7.— Viewing angles  $\theta$  and  $\phi$  represent the angles between the principal axes, a, b, and c, and the viewing axes, x, y, and z, as shown. The z axis is chosen to be along the line of sight, putting the x and y axes in the sky plane.  $\psi$  is apparent angle between the projection of the minor axis (y) and the short principal axis, c, on the sky.

$\theta$ , there is a maximum possible  $\phi$ . This restricts the range of values to those shaded in Figure 8. Modelling has shown that choosing the maximum  $\phi$  value puts the figure rotation axis approximately perpendicular to the slit at p.a. of  $132 \pm 2^\circ$ , and  $\beta = 81 \pm 2^\circ$ . We can therefore constrain the figure rotation (long) axis to be between  $107^\circ$  and  $132^\circ$ ; we (arbitrarily) adopt the midpoint of  $119^\circ$ , which gives  $\beta = 68^\circ$ .

The dust lane lies in the plane perpendicular to the radio axis (see section 4.1.1).  $\theta$  can be chosen to reproduce the apparent tilt of the dust lane in the perpendicular plane. The warp in the dust lane makes the tilt difficult to judge, but within the range  $60^\circ < \theta < 80^\circ$ , modelling suggests  $\theta = 65^\circ$ . For  $\beta = 68^\circ$ ,  $\phi$  is found to be  $19 \pm 1^\circ$ .

Once the angles are decided, the dependence of the axis ratios is shown in Figure 9. The intrinsic ratio  $C/A \geq 1/2$  is implied by the small number of radio galaxies flatter than E5 (Hummel 1980, referenced in van Albada et al. 1982). Therefore  $0.5 < \xi < 1$  and  $\zeta > \xi$ . The choice of  $\zeta$  and  $\xi$  affect the apparent photometric major/minor axes ratio. Saripalli et al (1994) found this axis ratio to be 1.18. Modelling

an ellipsoid with  $\zeta = 0.75 \pm 0.05$  and  $\xi = 0.69 \pm 0.06$  at the chosen angles was found to reproduce this major/minor axis ratio, giving  $1.18 \pm 0.01$ .

Figure 10 shows our adopted model for ESO248-G10 with  $\psi = 34^\circ$ ,  $\theta = 65^\circ$ ,  $\phi = 19^\circ$ ,  $\zeta = 0.75$ , and  $\xi = 0.69$ . While not the only possible model, it does represent a self consistent choice of angles and it reproduces the observed features.

## 4.2. Nature of the Nuclear Source and Circumnuclear Structure

### 4.2.1. Reddening Processes

The extinction images in Figure 2(d) reveal significant reddening around the nucleus. Thermal gas emission, hot dust emission and dust extinction can all affect the galaxy colours. To distinguish between these processes, the two-colour pixel plot in Figure 11 was formed from the values of  $31 \times 31$  pixels ( $15.5 \times 15.5$  arcsec) around the nucleus; the typical colours of E/S0 galaxies and QSOs are shown on the figure. Also shown are vectors representing 5 magnitudes of visual extinction, hot dust at temperatures

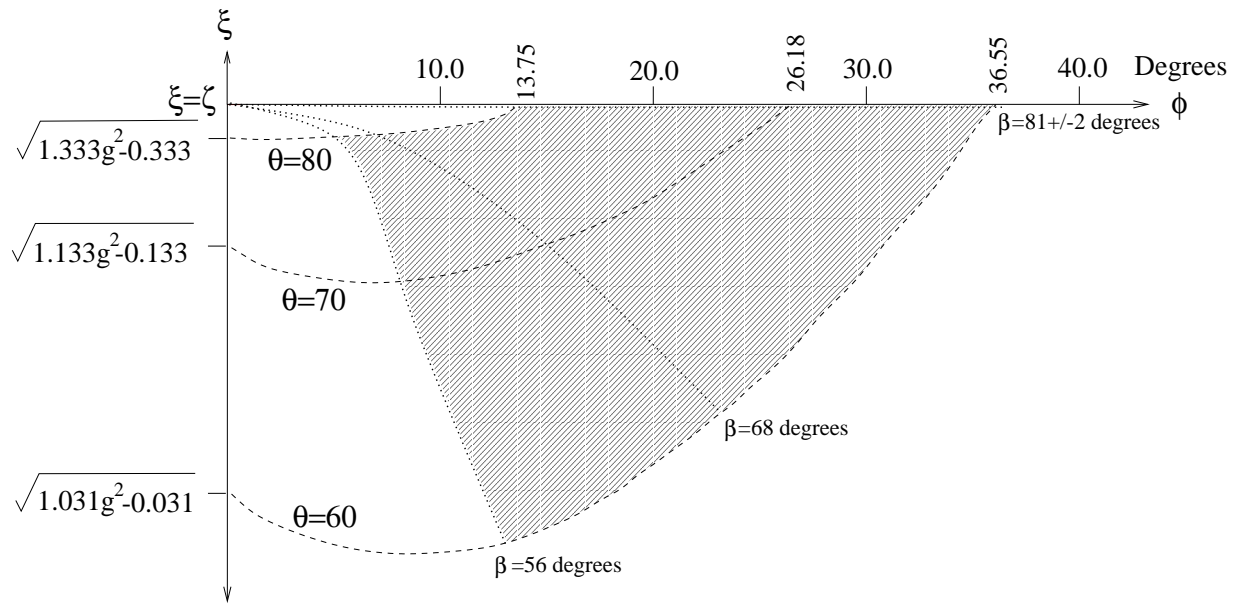


Fig. 8.—  $\xi$  vs  $\phi$ . The shaded region represents the range of values allowed by equation 1 and the constraint  $\zeta > \xi$ , for the chosen range of  $\theta$ .

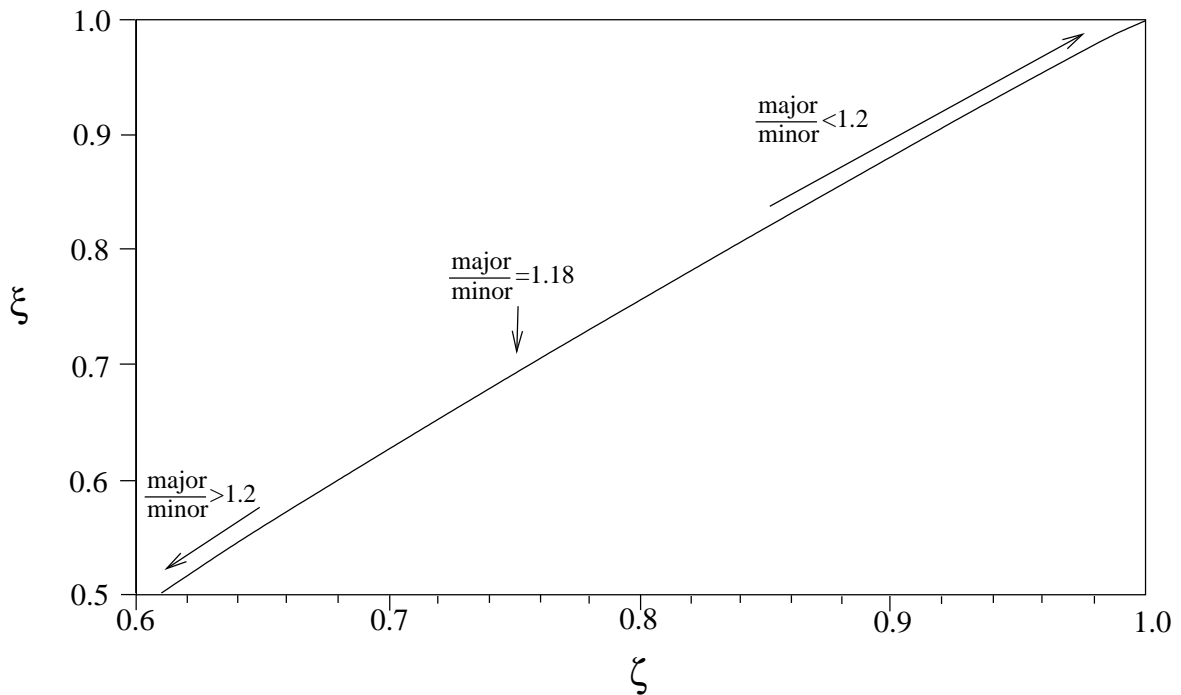


Fig. 9.—  $\xi$  vs  $\zeta$  for the chosen values of  $\theta$ ,  $\psi$ , and  $\phi$ . The apparent major-to-minor axis ratio is dependent on  $\xi$  and  $\zeta$  as shown.

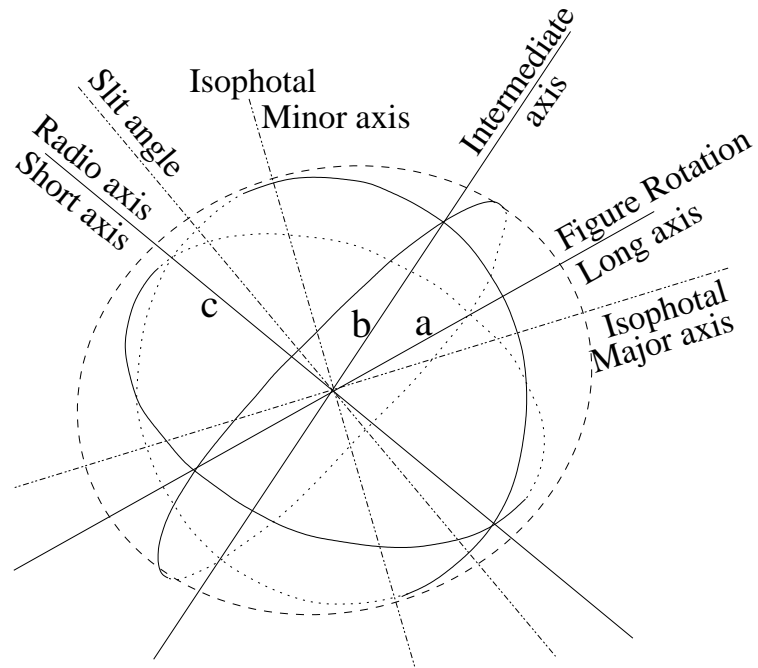


Fig. 10.— A model for the orientation of ESO248-G10. The angles are  $\theta = 65^\circ$ ,  $\psi = 34^\circ$ ,  $\phi = 19^\circ$ , and axis ratios of  $B/A = 0.75$  and  $C/A = 0.69$ .

of 800 and 1000K mixed with a late-type stellar population, and thermal gas comprised of hydrogen and helium continuum and emission lines mixed with late-type stars (Alonso-Herrero et al. 1998). Aperture photometry colours for a range of increasing apertures are also plotted in Figure 11.

Notice that in Figure 11 both the individual points coincident with the nucleus and the smallest aperture photometry point are bluer than points at larger radii. With increasing radius, the colours initially become redder along an almost horizontal vector. Beyond a radius of 4 arcsec, the points then follow the direction of the hot gas vector. Two scenarios could explain this pattern. The colours may be the sum of a hot dust and a hot gas vector. As the radius increases, the contribution of the hot dust and hot gas both grow until, at 5 arcsec, the hot gas processes become dominant and there is no further contribution from hot dust. Similarly, dust extinction, not emission, could contribute to reddening out to 5 arcsec. From the two-colour pixel plot alone, it is not possible to distinguish between these two scenarios and we now examine in turn the evidence for dust extinction and hot dust emission.

(a) *Dust extinction*: This is plausible since the optical images clearly show a dust lane. The thickest portion of the dust lane does not appear to obscure our view of the nucleus, as the tilt results in the foreground dust passing above the nucleus. Two observations support the interpretation of the two-colour pixel plot as indicating dust extinction plus thermal gas. Firstly, the nuclear pixels do not show as much dust extinction as those at larger radius. Secondly, the aperture photometry colours follow a dust extinction plus thermal gas emission vector until the 4 arcsec aperture point. This corresponds to the distance to which the dust lane extends from the nucleus in the direction where the dust lane is closest to the nucleus in the optical images. Beyond 4 arcsec, the aperture photometry points follow the thermal gas vector and show no further contribution from dust extinction. Furthermore, the individual points within the dotted circle in Figure 11, which have the highest reddening, are the pixels on the dust lane; dust extinction provides a logical explanation for these points. If so, the extinction to the dust lane pixels would be around 13 visual magnitudes.

(b) *Hot dust emission*: The second explanation of the

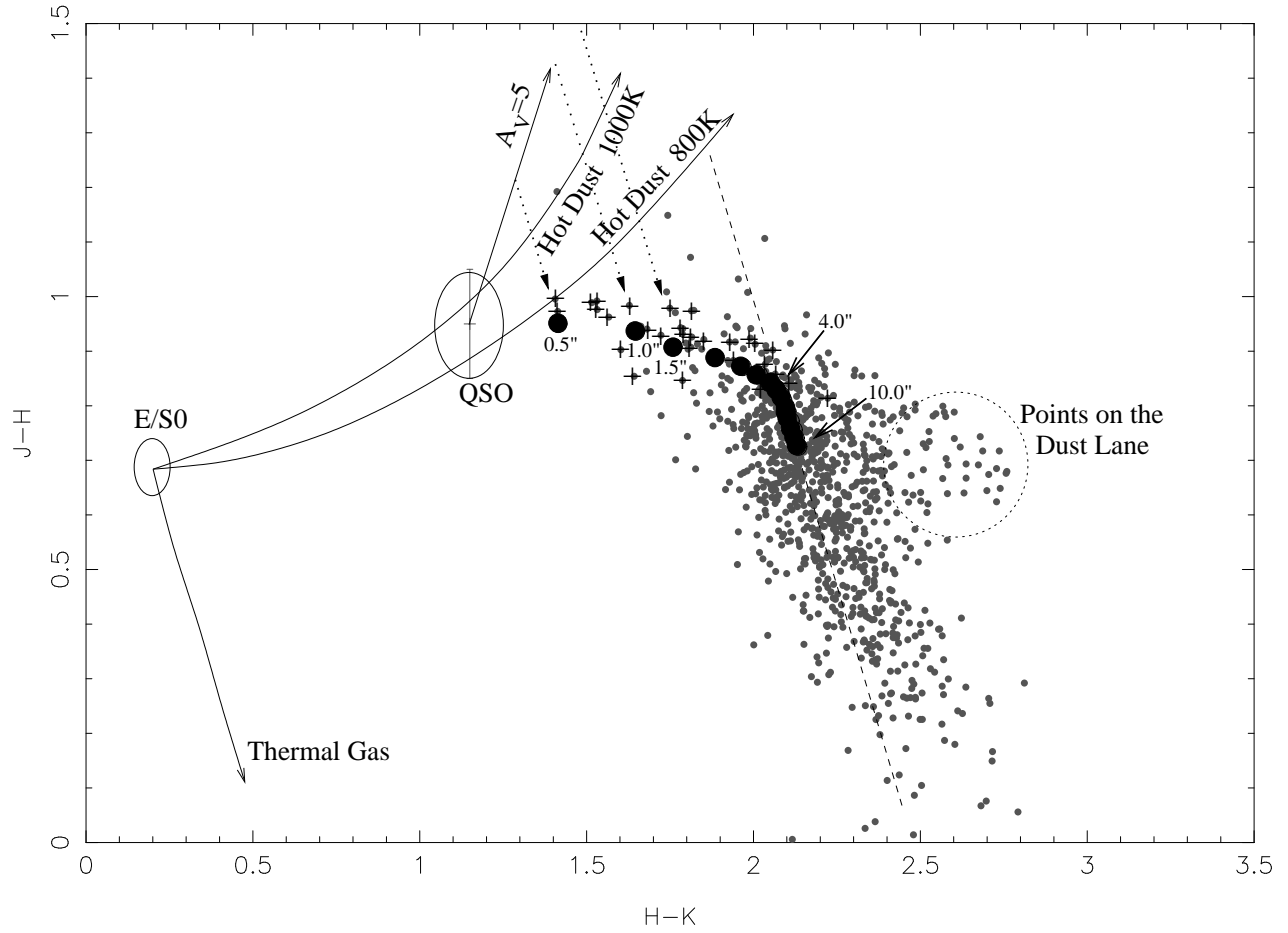


Fig. 11.—  $J - H$  vs  $H - K$  for ESO248-G10. Typical elliptical galaxy and QSO colours are marked by the two ellipses. An extinction vector of  $A_V = 5$  is shown along with hot dust vectors for 800K and 1000K. The colours of  $31 \times 31$  pixels ( $15.5 \times 15.5$  arcsec) centred on the nucleus are shown by the small dots. The crosses are the 30 pixels closest to the nucleus. Aperture photometry colours marked by large dots represent apertures of 0.5, 1, 1.5, 2, 2.5, 3, 3.5, 4, 4.5, 5, 6, 7, 8, 9, 10 arcsec from left to right. For clarity only some of these aperture radii have been labelled. Points within the dotted circle all lie on the dust lane. The dashed line is parallel to the thermal gas vector. Dotted lines indicate a thermal gas vector which could combine with the dust extinction or hot dust vectors to give the observed aperture photometry points.

two-colour pixel plot involves hot dust emission as the prominent reddening source out to 4 arcsec. Four mechanisms may contribute to hot dust emission: (i) transient heating of small grains by reprocessed X-rays, (ii) scattered nuclear radiation, (iii) heating by UV photons from the central source, or (iv) in situ heating of dust by hot stars. We now examine each mechanism in turn. The first option cannot be ruled out in this case, as models of X-ray heating of small grains are inconclusive. The processes of grain destruction and heating are not well enough understood to produce consistent models of this process. For the second mechanism, hot dust emission close to the central source can be scattered into the line of sight by clouds further from the nucleus. A polarisation image would be required to prove scattering. However, models of similar galaxies have shown that essentially all the emission would need to be scattered towards the line of sight (Alonso-Herrero et al. 1998). Hence, this scattering scenario is unlikely. The third mechanism for hot dust emission is heating by UV photons from the central source which will reradiate in the near infrared. UV heating has been considered to be a major source of near-infrared emission from regions close to the nuclei of Seyfert galaxies (Alonso-Herrero, Ward & Kotilainen 1996; Kotilainen et al 1992; Bryant & Hunstead 1999). If the same process is responsible for extended thermal dust, then it must be shown that UV photons from the central source can heat the dust to the observed temperatures out to the radius required. For a dust optical depth of  $\tau_{UV}$ , a total UV luminosity of  $L_{UV}$  (in units of  $10^{46} \text{ erg s}^{-1}$ ) would heat the dust to a temperature  $T$  (K) out to a radius  $r$  (pc) given by,

$$T = 1650 \left( \frac{L_{UV}}{r^2} \cdot e^{-\tau_{UV}} \right)^{\frac{1}{5.6}} \quad (6)$$

(Barvainis 1987). The near-infrared colours indicate that if hot dust is the reddening mechanism, then this dust extends to  $\sim 6.5 \text{ kpc}$  ( $\sim 4 \text{ arcsec}$ ) before hot gas becomes the dominant mechanism. The typical temperature for such hot dust is around 800K. A higher temperature would produce a steeper vector on the 2-colour plot. At 1500K the dust would be evaporated by the UV radiation (Barvainis 1987). Therefore, to heat dust to a temperature of 800K out to a radius of 6.5 kpc would require a UV luminosity of  $1.5 \times 10^{51} \text{ erg s}^{-1}$ , three orders of magnitude greater than the most luminous quasars. Therefore, it is very unlikely that UV radiation from the central source could be responsible for heating dust to such a radius.

The fourth origin of hot dust emission requires groups of hot stars to provide local heating of the dust far from the central source. Massive star formation in the galaxy halo produces UV emission which can be almost entirely converted to thermal dust radiation (Alonso-Herrero et al. 1998). Not only can star forming regions heat the dust, they can also heat the gas. As thermal gas emission is an important processes further from the nucleus, the evidence for starburst regions will be discussed at length in the next section. The star forming regions will be shown to extend to the radius of the proposed hot dust emission.

#### 4.2.2. Distribution of AGN and Starburst Processes

Table 4 compares three diagnostic emission line ratios measured in 3 pixels (2.3 arcsec) centred on the nucleus with the expected ratios for starbursts and AGNs (Radovich & Rafanelli 1996, Hill et al. 1999). For each diagnostic, the nucleus is clearly identified with AGN emission.

In Figure 1(d), horizontal lines represent five regions where pixels were extracted to make spectra. The corresponding spectra and the  $[\text{N II}]\lambda 6584/\text{H}\alpha$  flux ratios are shown below the rotation curve. For radii less than  $\sim 5 \text{ arcsec}$  from the nucleus, the ratio is  $> 1.2$  as required for AGNs. However, beyond this radius, the ratios drop to the range expected for starburst/composite regions ( $\leq 0.8$ ). Therefore, star formation regions are found beyond the radius at which the slow rotation ‘dip’ (see section 3.2.2) starts on the rotation curve. It is notable that whereas the slow rotation ‘dip’ is only seen to the north-east of the nucleus, the evidence of star formation begins at the same radius to both the north-east and south-west.

#### 4.2.3. North-east ‘Dip’ in Rotation Curves

Rotation curve features similar to the north-east velocity ‘dip’ have been observed in other galaxies. In each case, however, the explanation for the dip does not appear relevant to ESO248-G10. Ionised gas rotation curves with a steep gradient followed by a dip then a shallower gradient have in some cases (eg: NGC253 Arnaboldi et al. 1995) been attributed to a nuclear ring. Capaccioli & Longo (1994) suggest that stellar rotation curves with a sharp rise up to a maximum followed by a dip then a shallower rise, are typical of lenticular galaxies (eg: NGC1553, an S0 galaxy), in which the dip marks the transition between disk-dominated and bulge-dominated parts of

Table 4: Measured emission line ratios for three diagnostic emission line pairs, measured at the nucleus.

Line Ratio	Measured value	Value for pure starburst	Value for AGN
$\frac{[N\,II]\lambda 6584}{H\alpha}$	$2.2 \pm 0.2$	$\leq 0.6$	$\geq 1.2$
$\frac{[S\,II]\lambda 6716+6731}{H\alpha}$	$0.73 \pm 0.2$	$\leq 0.25$	$\geq 0.32$
$\frac{[O\,I]\lambda 6300}{H\alpha}$	$0.18 \pm 0.05$	$\leq 0.05$	$\geq 0.1$

the galaxy. However, although the ESO248-G10 rotation curve shows a dip to the north-east, the lack of a corresponding dip to the south-west appears to rule out a nuclear ring or lenticular galaxy features. We now examine alternative models which include a second velocity system to the north-east.

#### 4.3. Possible Models of the Host Galaxy

A common source of extended emission line gas in ellipticals is capture from a merger or interaction with a gas rich galaxy (see section 4.1.1). In Figure 12(a) the  $R$  image has been divided by the  $B$ , to give an  $B - R$  image in which darker regions correspond to redder colours. The nucleus has  $B - R = 2.5$  and is marked by a cross. Approximately 10 arcsec to the east of the nucleus is a bluer patch with  $B - R = 1.3$ , first identified by Saripalli et al. (1994). This could be a merging companion or a region of blue stars. The blue patch appears to be extended towards the west.  $J$ -band contours overlaid on the  $B - R$  image appear unaffected by the dust lane to the north-west of the nucleus. It is therefore likely that the distortion of the  $J$ -contours to the east, whilst coincident with the dust lane, is due to the extended emission associated with the blue patch rather than dust.

If the blue region in ESO248-G10 can be identified with an interacting companion, then its orbit will be settling into the principal plane closest to the angular momentum vector of the merging galaxy (see section 4.1.1). In Figure 12(b), the p.a. of the blue patch from the galaxy nucleus is between the figure rotation axis and the radio axis. In fact, it could be closer to either. If the merging galaxy is in the long/intermediate plane, and settling into an orbit about the radio axis, then the current merger could be responsible for the warped dust lane. While that

hypothesis can not be ruled out, it would not support the distribution of starburst regions or the rotation curve features observed.

An alternative picture involves the merging galaxy being located in the short/intermediate plane and hence settling into rotation with the figure and gas orbits. The dashed lines in Figure 12(b) are two orbits about the figure rotation axis, projected onto the sky plane. Their radii were chosen to lie at either end of the putative merging galaxy. In Figure 1(c), a region of slower velocity was evident from a radius of  $\sim 5 - 15$  arcsec to the north-east, with a local minimum at a radius of  $\sim 8$  arcsec from the nucleus. A white line along the slit direction in Figure 12(b) marks the radii of the ‘dip’, with the cross line at the local minimum velocity. If gas is being accreted from the blue galaxy into an orbit about the figure axis, the radii of this gas when rotated to the apparent slit angle, corresponds well with the slower gas region. However, it is likely that the merging galaxy would have an orbit close to the one shown, but not yet settled into the short/intermediate plane. Nevertheless, if the blue region is a merging companion, then it could be the second velocity system affecting the rotation curve. This picture suggests the inner radius of the proposed merging galaxy’s orbit is currently  $\sim 5$  arcsec. Hence the radius at which thermal gas is accreted into the orbit should be the same either side of the nucleus. Newly accreted gas has not yet merged with the orbiting gas and could lead to a second velocity system near the merging galaxy. Therefore only the north-east of the rotation curve is affected by a second velocity system. The gas is heated by star-forming regions triggered by the merger. The detection of starburst emission line ratios should therefore be symmetric about the nucleus. This symmetry was indeed observed in Figure 1(d), where starburst line

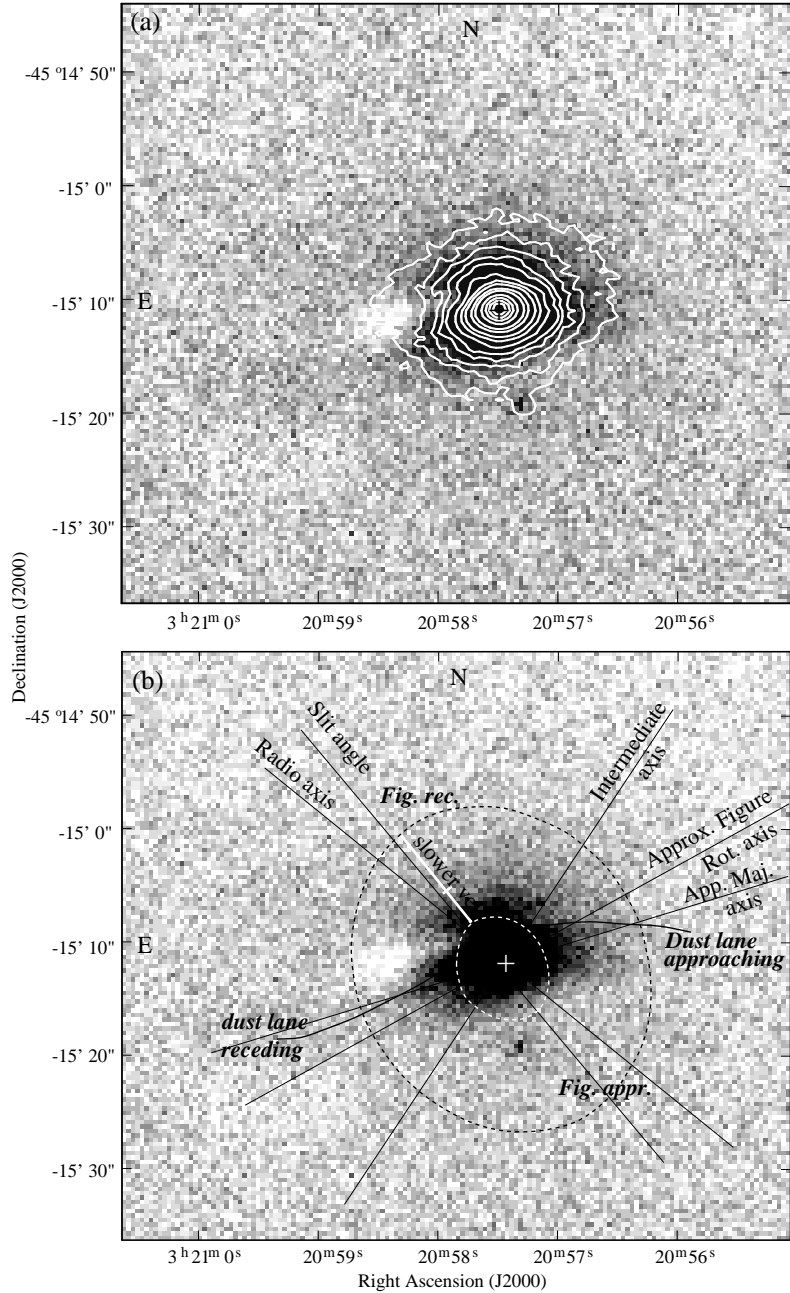


Fig. 12.— (a)  $B - R$  image overlaid with J-band contours. The nucleus is marked by the cross. Darker regions represent redder colours. There is clearly a blue region to the east of the nucleus. Contour levels are 17.9, 18.1, 18.4, 18.7, 19.1, 19.3, 19.7, 19.9, 20.1, 20.4, 20.9, 21.2, 21.6 mag pixels<sup>-1</sup>. The J-band has distorted contours along the westward extension of the blue patch to the west. This is unlikely to be due to the dust lane as it is not apparent in the contours on the west side of the galaxy. (b)  $B - R$  image with axes marked. The white line along the slit position angle, defines the radii (5-15 arcsec) of the slower velocity ‘dip’ from the rotation curve. The local minimum velocity in the ‘dip’ is marked by the perpendicular dash across the white line. Two orbits about the figure rotation axis are shown by the dashed lines, with radii chosen to lie at either end of the blue feature. Rotation in this sense would map the blue feature onto the region of slower velocity (see section 4.3).

ratios became dominant over AGN processes beyond  $\sim 5$  arcsec on both sides of the nucleus.

An alternative explanation could involve the gas originating from a previous merger, and the blue region as a cluster of stars. This, however, would leave no evidence in any of the images, for the source of the second velocity system. Interpretation of the blue region as merging galaxy provides a self-consistent explanation of the observed gas rotation, starburst distribution, and optical colours.

## 5. FUTURE WORK

Optical images in better seeing would help to resolve the dust lane features and the proposed merging galaxy. Observations to test the interpretation of the blue region as a merging galaxy are currently planned, including spectral mapping to measure the dynamics and distribution of gas across the galaxy. The resulting spectra across the dust lane may confirm the sense of the dust rotation. Furthermore, the rotation information across the galaxy would refine the axis of gas rotation and our model for the orientation of ESO248-G10.

The radio axis position angle was assumed to be that of the radio jets far from the nucleus as mapped by Saripalli et al. (1994). However, there is evidence that the jet direction may be changing systematically with time, possibly indicating precession, and hence may not be at exactly the same position angle as further out. Therefore, a detailed radio map of the core regions at arcsec resolution could constrain the local radio jet position angle and hence further constrain the angles found from modelling the system.

In section 3.2.1 it was shown that there is no [Fe II] within 1.6 arcsec of the nucleus, where AGN processes dominate. This may indicate that if iron is present and not excited by the AGN, then in general, iron excitation may be more likely from starburst processes: in cooling tails of SNRs or photoionized by young OB stars. An [Fe II] image and a higher resolution radio image of ESO248-G10 could be used to test the excitation mechanism for [Fe II] in active galaxies. The emission should be more prominent at a radius  $> 5$  arcsec (see section 4.2.2) if it is due to starburst processes. Furthermore, a correlation between the line image and the radio image would be expected for excitation in cooling tails of SNRs.

## 6. CONCLUSION

ESO248-G10 has been modelled as a triaxial ellipsoid with axes ratios of  $B/A = 0.75$  and  $C/A = 0.69$ , oriented with angles  $\psi = 34^\circ$ ,  $\theta = 65^\circ$ , and  $\phi = 19^\circ$ . This is not an exclusive solution but one that is consistent with the observed apparent axes and rotation angles. The core has been identified as an AGN, surrounded by either hot dust emission or dust extinction. Hot gas has been found to play an increasing role beyond a radius of 4 arcsec (6.5 kpc). An optical spectrum has revealed fast gas rotation out to a radius of 20 arcsec ( $\sim 33$  kpc). A slower velocity region extending from a radius of 5 to 15 arcsec to the north-east has been identified as a second velocity feature. A model is proposed in which this feature is a merging gas-rich galaxy, which is inducing star formation as it settles into an orbit about the figure rotation axis.

## ACKNOWLEDGMENTS

We would like to thank Oak-Kyoung Park for taking the *J* and *H*-band CASPIR images for us, and Elaine Sadler for helpful discussions and comments on an earlier draft of the paper. This research has been supported in part by a grant from the Australian Research Council.

## 7. BIBLIOGRAPHY

- Allen, D. 1992, Proc. Astron. Soc. Aust., 10, 94
- Alonso-Herrero, A., Simpson, C., Ward, M. J. & Wilson, A. S. 1998, ApJ, 495, 196
- Alonso-Herrero, A., Ward, M. J. & Kotilainen, J. K. 1996, MNRAS, 278, 902
- Arnaboldi, M., Capaccioli, M., Cappellaro, E., Held, E. V. & Koribalski, B. 1995, AJ, 110, 199
- Barvainis, R. 1987, ApJ, 320, 537
- Bertola, F., Buson, L. M. & Zeilinger, W. W. 1992, ApJ, 401, L79
- Binney, J. 1978, MNRAS, 183, 779
- Bryant, J. J. & Hunstead, R. W. 1999, MNRAS, 308, 431
- Capaccioli, M., Cappellaro, E., Held, E. V. & Vietri, M. 1993 A&A, 274, 69
- Capaccioli, M. & Longo, G. 1994, ARA&A, 5, 293
- Carballo, R., Sanchez, S. F., Gonzalez-Serrano, J. I., Benn, C. R. & Vigotti, M. 1998, AJ, 115, 1234
- de Zeeuw, P. T. & Franx, M. 1989, ApJ, 343, 617
- Fanaroff, B. L. & Riley, J. M. 1974, MNRAS, 167, 31
- Fisher, D., Illingworth, G. & Franx, M. 1994, AJ, 107,

Gooch, R. 1996, ADASS, 5, 80

Hawarden, T. G., Elson, R. A. W., Longmore, A. J., Tritton, S. B. & Corwin Jr., H. G. 1981, MNRAS, 196, 747

Heckman, T. M., et al. 1986, ApJ, 311, 526

Hill, T. L., Heisler, C. A., Sutherland, R. & Hunstead, R. W. 1999, AJ, 117, 111

Hui, X., Ford, H. C., Freeman, K. C. & Dopita, M. A. 1995, ApJ, 449, 592

Jones, P. A. 1989, PASA, 8, 81

Kormendy, J. & Djorgovski, S. 1989, ARA&A, 27, 235

Kotanyi, C. G. & Ekers, R. D. 1979, A&A, 73, L1

Kotilainen, J. K., Ward, M. J., Boisson, C., DePoy, D. L., Bryant, L. R. & Smith, M. G. 1992, MNRAS, 256, 149

Merritt, D. & de Zeeuw, T. 1983, ApJ, 267, L19

McGregor, P., Hart, J., Dowling, M., Hoadley, D. & Bloxham, G. 1994, ExA, 3, 139

Mollenhoff, C., Hummel, E. & Bender, R. 1992, A&A, 255, 35

Nicholson, R. A., Bland-Hawthorn, J. & Taylor, K. 1992, ApJ, 387, 503

Radovich, M. & Rafanelli, P. 1996, A&A, 306, 97

Saripalli, L., Subrahmanyan, R. & Hunstead, R. 1994, MNRAS, 269, 37

Sault, R. J., Teuben, P. J. & Wright, M. C. H. 1995, ADASS, 4, 433

Shortridge, K. 1993, in ASP Conf. Ser. 52, Astronomical Data Analysis Software and Systems II, ed. R. J. Hanisch, R. J. V. Brissenden & J. Barnes (San Francisco: ASP), 219

Stark, A. A. 1977, ApJ, 213, 268

Steiman-Cameron, T. Y. & Durisen, R. H. 1982, ApJ, 263 L51

Steiman-Cameron, T. Y., Kormendy, J. & Durisen, R. H. 1992, AJ, 104, 1339

Surace, J. A. & Sanders, D. B. 1999, ApJ, 512, 174

Tody, D. 1993, in ASP Conf. Ser. 52, Astronomical Data Analysis Software and Systems II, eds. R. J. Hanisch, R. J. V. Brissenden, & J. Barnes (San Francisco: ASP), 173

van Albada, T. S., Kotanyi, C. G. & Schwarzschild, M. 1982, MNRAS, 198, 303